RESEARCH ARTICLE

ADVANCED MATERIALS
www.advmat.de

Temperature Invariant, Nearly Zero Temperature Coefficient of Resistivity in Si-Doped Titanium Nitrides

*S. Novia Berriel, Corbin Feit, Md. Rafiqul Islam, Jia Shi, Somilkumar J. Rathi, Ajit Dhamdhere, Hae Young Kim, Patrick E. Hopkins, Talat Rahman, Duy Le, and Parag Banerjee**

Materials with near-zero temperature coefficient of resistivity (nz-TCR) are critical for precision electronics operating across wide temperature ranges, yet achieving ultra-stable resistivity remains a challenge. Here, a mixed nitride Ti—Si—N thin film system is demonstrated exhibiting exceptional nz-TCR stability (0.05 ppm K^{-1}) from 80 to 420 K, realized through atomic-level control of electron scattering mechanisms. By tuning Si content in TiN (2–4 at%), a TCR transition from metallic (positive) to insulating (negative) behavior is induced, with optimal stability at $Ti_{0.98}Si_{0.02}N$. Atomic layer deposition enables precise synthesis, while structural, electronic, and thermal characterization, supported by density functional theory-based calculations, reveal that nz-TCR arises from a control of elastic mean free path and average diffusion length of electrons. The elastic mean free path (0.712 nm) approaches the lattice parameter (0.455 nm), and the average diffusion length (5.5 nm) aligns with the size of Si decorated grains (5.66 nm), thus leading to temperature invariant electronic transport. This work provides a generalizable design principle for ultra-stable nz-TCR resistors using composition control and grain-boundary engineering.

1. Introduction

Electrical resistivity (ρ) is a property that exemplifies the flow and collective behavior of electrons in a material. Temperature coefficient of resistivity (TCR) is the parameter that quantifies the variability of ρ as a function of T. Generally speaking, TCR >0 in a metal because of increased scattering processes that results in an increase in ρ as T increases.[1] On the other hand, TCR <0 broadly defines insulators, amorphous metals, and disordered alloys.[2] Transitioning across these two categories is the intriguing regime of a nz-TCR material, which demonstrates minimal resistivity change with T. Foil resistors,[3] antiperovskites,[4–6] and nanocomposites[7–10] with individual components of opposing TCRs, have all demonstrated nz-TCR behavior. From an applications perspective, nz-TCR materials are attractive candidates for use in wearable strain sensors,[11,12] and resistors[7] in quantum and microelectronics.

The nz-TCR behavior is governed by the empirical Mooij rule,[13] which predicts that TCR ≈0 behavior emerges for materials with ρ of 100–150 µΩ cm. The rule can be explained by recognizing that ρ in conductors is related to the elastic electron mean free path, l_e. At temperatures where l_e approaches the fundamental limit of interatomic spacing "a_o," ρ saturates and becomes independent of

---

S. N. Berriel, C. Feit, P. Banerjee
Department of Materials Science and Engineering
University of Central Florida
Orlando, FL 32816, USA
E-mail: parag.banerjee@ucf.edu

M. R. Islam, P. E. Hopkins
Department of Mechanical Engineering and Aerospace Engineering
University of Virginia
Charlottesville, VA 22904, USA

J. Shi, T. Rahman, D. Le
Department of Physics
University of Central Florida
Orlando, FL 32816, USA

S. J. Rathi, A. Dhamdhere, H. Y. Kim
Eugenus Inc.
677 River Oaks Parkway, San Jose, CA 95134, USA

The ORCID identification number(s) for the author(s) of this article can be found under https://doi.org/10.1002/adma.202514483

DOI: 10.1002/adma.202514483

P. E. Hopkins
Department of Materials Science and Engineering
University of Virginia
Charlottesville, VA 22904, USA

P. E. Hopkins
Department of Physics
University of Virginia
Charlottesville, VA 22904, USA

T. Rahman, D. Le, P. Banerjee
REACT Faculty Cluster
University of Central Florida
Orlando, FL 32816, USA

P. Banerjee
Nano Science and Technology Center
University of Central Florida
Orlando, FL 32816, USA

P. Banerjee
Florida Solar Energy Center
University of Central Florida
Orlando, FL 32816, USA

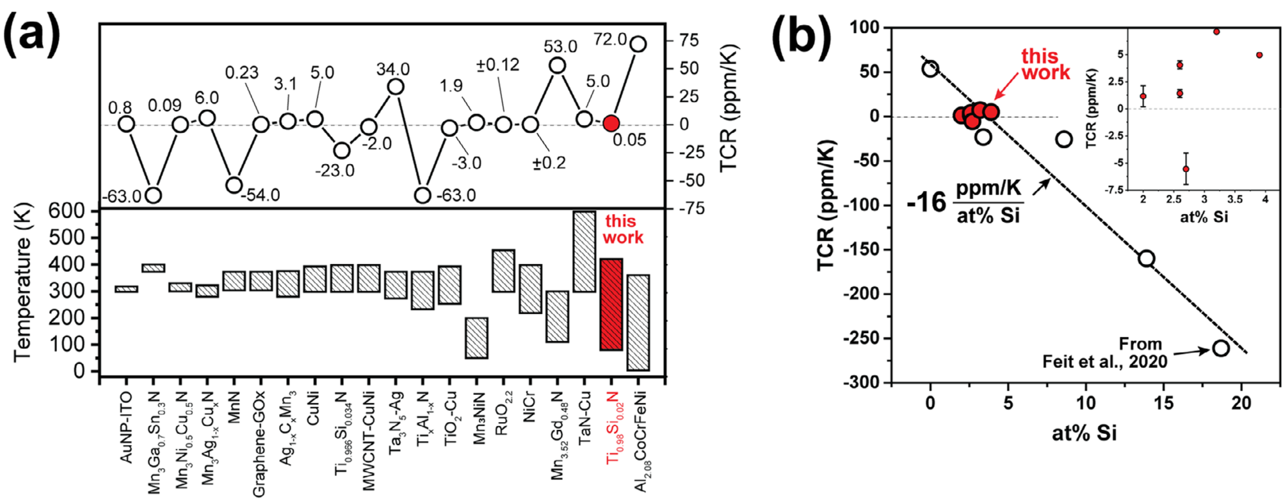

Figure 1. a) Survey of nz-TCR materials (*x*-axis) – top graph; and the corresponding temperature range within which nz-TCR is demonstrated–bottom graph. Data has been organized as a function of increasing temperature range, from left to right. All references cited in text. Data from the current work is highlighted in red. b) Variation of TCR as a function of at% Si in $Ti_{[1-(x/100)]}Si_{(x/100)}N$. The open symbols are from Feit et al.,[21] and the filled symbols correspond to this work. The region between 2–4 at% Si provides a series of samples with nz-TCR.

temperature. This condition is known as the Mott-Ioffe-Regel (MIR) limit.[14,15]

Maintaining the thermal stability of nz-TCR has been a long-standing challenge. This behavior is underscored in **Figure** 1a that summarizes nz-TCR materials reported till date.[3–6,8–10,12,16–26] The top graph reports the TCR (in ppm K^{-1}) while the bottom graph shows the upper and lower temperatures and range ΔT, in which nz-TCR behavior is exhibited. For example, solution-processed nanoparticle thin films[12] show a TCR of 0.799 ppmK^{-1}. However, the $\Delta T = 20$ K only. On the other hand, vacuum arc remelted high-entropy alloy[26] $Al_{2.08}$CoCrFeNi has a non-trivial TCR of 72 ppmK^{-1} and a wide ΔT = 355.8 K. Thus, it is challenging to obtain low nz-TCR behavior with the widest temperature regime of stability.

Herein, we report a mixed nitride $Ti_{0.98}Si_{0.02}N$ with an nz-TCR of 0.05 ppmK^{-1} stable from 80–420 K, i.e., a temperature range of ΔT = 340 K. This is highlighted in red in Figure 1a. The development of the $Ti_{0.98}Si_{0.02}N$ composition with the desired nz-TCR behavior is arrived through our previous work,[21] where the TCR of a range of $Ti_{[1-(x/100)]}Si_{(x/100)}N$ compositions (0%≤ x ≤24.2%) were reported as open symbols shown in Figure 1b. According to this graph, a crossover in TCR is to be expected between 2–4 at% Si. By synthesizing films within this targeted composition range, a cluster of TCR values were indeed generated with nz-TCR behavior as given in Figure 1b with filled symbols, while the inset shows the TCR averaged over triplicate samples for a given composition. Within the 1.16 ± 0.978 ppmK^{-1} sample set at 2 at% Si, one sample demonstrated a nz-TCR of 0.05 ppmK^{-1} as shown in Figure 1a. This paper discusses the detailed electrical, thermal, chemical, and structural characterization of the $Ti_{0.98}Si_{0.02}N$ films with ab initio calculations that lead to a detailed understanding of the mechanisms for nz-TCR behavior.

2. Results

2.1. Electrical and Thermal Transport

Figure 2a shows ρ for a 142.3 nm TiN film with temperature varying as, 80 K≤ T ≤420 K. The ρ_{80K} is 178.76 μΩ cm and remains unchanged till $T \approx 160$ K.[27] Thereafter, ρ increases where ρ_{300K} is 180.67 μΩ cm and is comparable to the reported ρ of polycrystalline TiN between 160–230 μΩ cm.[28] The variation of ρ as a function of temperature for $Ti_{0.98}Si_{0.02}N$ is shown in Figure 2b. The addition of Si to TiN film leads to an increase in resistivity.[21] Here ρ_{80K} = 304.78 μΩ cm, ρ_{300K} = 304.80 μΩ cm and ρ_{420K} = 304.74 μΩ cm. Notably, the variation of ρ is negligible and accounts for only a change of 0.021 % between 80 to 420 K.

The TCR is obtained as,[29]

$$TCR = \frac{1}{\rho_o}\left(\frac{d\rho}{dT}\right) \tag{1}$$

where ρ_o is the reference resistivity chosen to be the resistivity at the lowest temperature (80 K). TCR as a function of temperature for TiN is shown in Figure 2c. Between 80 K≤ T ≤160 K, the TiN TCR lies between −27.84 and 12.08 ppmK^{-1}. Thereafter, the TCR increases with temperature, reaching a value of 98 ppmK^{-1} at 300 K and 130 ppmK^{-1} at 420 K. TCR for $Ti_{0.98}Si_{0.02}N$ is shown in Figure 2d. Across the entire temperature range tested, i.e., 80 K≤ T ≤420 K, the TCR varies from a maximum of 1.61 ppmK^{-1} (at 320 K) to a minimum of −5.92 ppmK^{-1} (at 410 K). The average TCR across this range is 0.05 ± 0.9 ppmK^{-1}.

We continue to discuss electrical measurements using **Table** 1 and return to the discussion on thermal conductivity

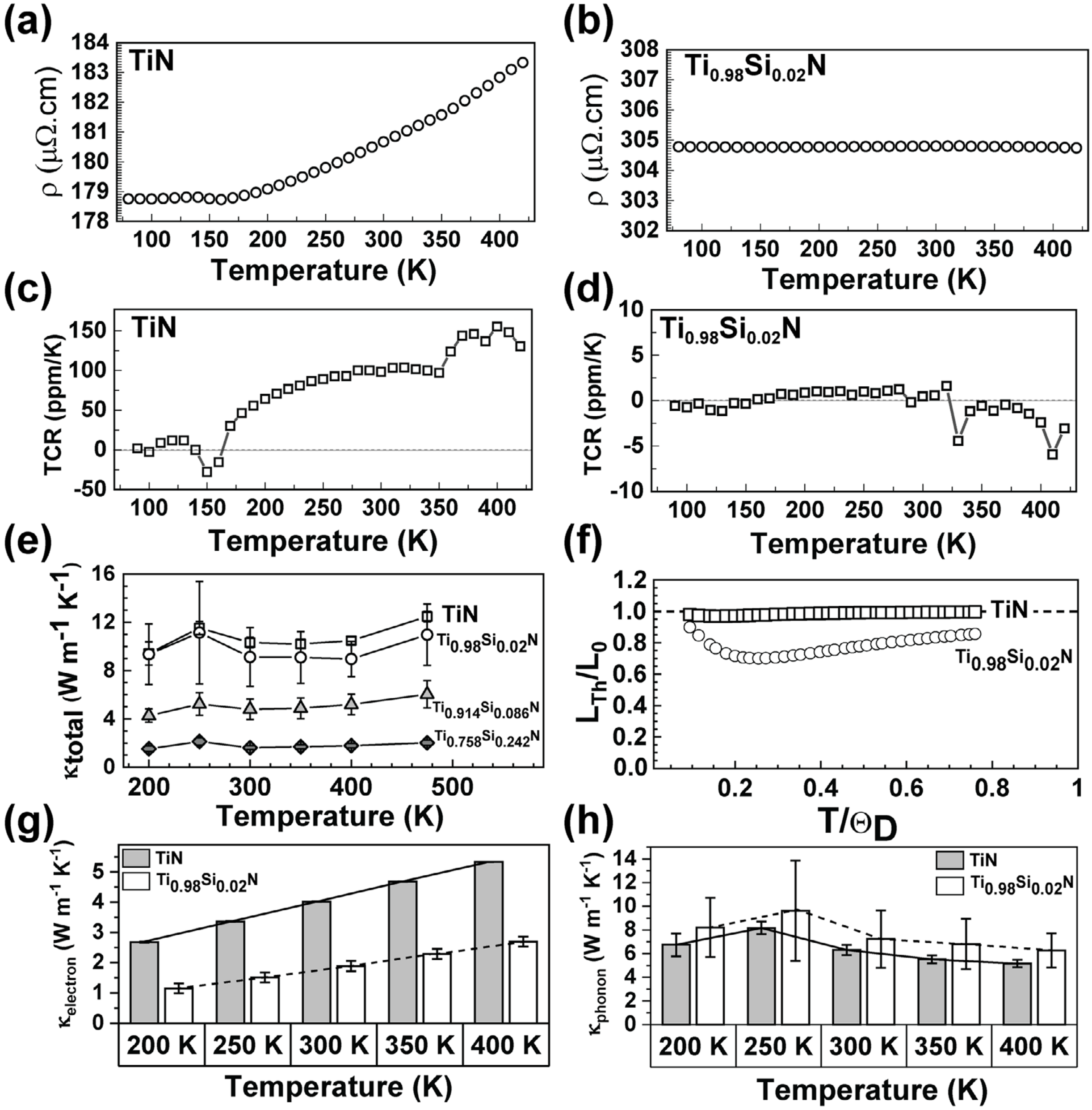

Figure 2. a) Change in ρ vs T for (a) TiN and b) $Ti_{0.98}Si_{0.02}N$ Note: y-axis range kept the same for both (a,b). Variation of TCR vs T for c) TiN and d) $Ti_{0.98}Si_{0.02}N$. e) TDTR measured the total thermal conductivity of TiN, $Ti_{0.98}Si_{0.02}N$, $Ti_{0.914}Si_{0.086}N$, and $Ti_{0.758}Si_{0.242}N$ films. f) Temperature-dependent theoretical Lorenz number (L_{Th}) to the Sommerfeld value (L_0), assuming, $\rho_{imp}/A = 0.1$ for TiN and $\rho_{imp}/A = 0.2$ for $Ti_{0.98}Si_{0.02}N$, $\Theta_D = 580$ K for both TiN and $Ti_{0.98}Si_{0.02}N$. g) Electron thermal conductivity vs T for TiN and $Ti_{0.98}Si_{0.02}N$. h) Lattice thermal conductivity vs T for TiN and $Ti_{0.98}Si_{0.02}N$.

Table 1. Table of at% Si, TCR, resistivity at 300 K (ρ_{300K}), carrier concentration at 300 K (n_{300K}), mobility at 300 K(μ_{300K}), and elastic mean free path at 300 K ($l_e|_{300K}$). Here, the room temperature resistivity uncertainty is 0.700 μΩ cm; Mobility uncertainty is ± 2 $cm^2\ Vs^{-1}$; Mean free path uncertainty is 0.002 nm. TCR listed is average over 80–420 K, and all other entries are room temperature (300 K) values for a representative sample out of 3 tested at each Si content.

at% Si	TCR [ppm K^{-1}]	ρ_{300K} [μΩ.cm]	n_{300K} [cm^{-3}]	$\mu_H\|_{300K}$ [$cm^2\ Vs^{-1}$]	$l_e\|_{300K}$ [nm]
0	76.80	180.7	8.52 x 10^{20}	40.56	7.787
2	0.05	304.7	1.41 x 10^{22}	1.46	0.712
2.6	1.41	309.2	3.41 x 10^{21}	5.91	1.803
2.7	5.73	318.6	6.14 x 10^{21}	3.19	1.183
3.9	4.96	333.4	9.91 x 10^{20}	18.90	3.816

as given in Figure 2e,f, subsequently. Hall measurements deconvolute two important parameters which contribute to film resistivity: 1) carrier concentration (n) and 2) Hall mobility (μ_H), where $\rho = (n e \mu_H)^{-1}$. Additionally, from this data the elastic mean free path (l_e) can be computed as,[30]

$$l_e = \frac{\left(r_s/a_o\right)^2}{\rho} \times 9.2\ \text{nm} \tag{2}$$

where, the r_s is the effective "radius of influence" of one free electron and given as, $r_s = \left(\frac{3}{4\pi n}\right)^{1/3}$ and, a_o is the Bohr radius. These data are collectively presented in Table 1 as a function of at% Si (determined by X-ray photoelectron spectroscopy (XPS) and shown below) including the average TCR (from 80–420 K), resistivity (ρ_{300K}), carrier concentration(n_{300K}), Hall mobility ($\mu_H|_{300K}$) and electron mean free path ($l_e|_{300K}$) - all at 300 K. The absolute value for TCR decreases from 76.80 ppmK^{-1} for TiN to 0.05 ppmK^{-1} for the $Ti_{0.98}Si_{0.02}N$. Further addition of Si to 3.9 at% maintains the low TCR value, and for $Ti_{0.961}Si_{0.039}N$ is only marginally higher at 4.96 ppmK^{-1}. The ρ_{300K} increases monotonically upon Si addition,[21] where for TiN = 180.7 μΩ cm and for $Ti_{0.961}Si_{0.039}N$ = 333.4 μΩ cm.

For TiN, room temperature free electron concentration (n_{300K}) is 8.52×10^{20} cm^{-3}. Upon addition of 2 at% Si, the n_{300K} increases by 16 × to 1.41×10^{22} cm^{-3}. This surprisingly high value signifies a maxima in free electron concentration in the Ti-Si-N system and can be compared to the value of epitaxially grown, single crystal TiN of 5×10^{22} by Johansson et al., and 8.3×10^{22} cm^{-3} by Gall et al.[31,32] Upon continued Si addition, the n_{300K} decreases and at 3.9 at% Si the $n_{300K} = 9.91 \times 10^{20}$ cm^{-3}. The $\mu_H|_{300K}$ follows an inverse trend, where TiN has a room temperature mobility of 40.56 cm^2 Vs^{-1}. This value drops to 1.46 cm^2 Vs^{-1} for the $Ti_{0.98}Si_{0.02}N$. Further increase in at% Si causes the $\mu_H|_{300K}$ to increase and for the $Ti_{0.961}Si_{0.039}N$ = 18.90 cm^2 Vs^{-1}.

The $l_e|_{300K}$ is given as the last column in Table 1. The TiN has a mean free path of 7.787 nm and significantly decreases to 0.712 nm for $Ti_{0.98}Si_{0.02}N$, which in turn approaches the lattice parameter value of 0.424 nm (determined with X-ray diffraction (XRD) and shown below). As Si at% increases, the mean free path increases to 3.816 nm for $Ti_{0.961}Si_{0.039}N$, similar to reported values.[33]

Time-domain thermoreflectance (TDTR) measurements were performed to understand the electron-phonon interactions in $Ti_{1-x}Si_xN$ ($0 \leq x \leq 0.242$) films as a function of temperature (200 K≤ T ≤475 K). Figure 2e shows that the total thermal conductivity is highest for TiN, followed by $Ti_{0.98}Si_{0.02}N$, $Ti_{0.914}Si_{0.086}N$, and lowest for $Ti_{0.758}Si_{0.242}N$ films due to an increase in electron and phonon scattering in the presence of Si.[34–36] Within one sample, an increase in thermal conductivity with increasing temperature is consistent with prior observations.[37–39] However, the overall reduction in thermal conductivity of TiN with the addition of 2 at% Si is minor and falls within the uncertainty range of TiN. This suggests a non-negligible phonon contribution to the thermal conductivity of $Ti_{0.98}Si_{0.02}N$, indicating that the reduction in electronic thermal conductivity does not affect the total thermal conductivity of these films within our experimental uncertainty.

To understand the thermal conductivity change that arises from the addition of Si in TiN, we analyze the electron component of thermal conductivity through a temperature-dependent Lorenz number calculation. The temperature-dependent theoretical expression for the Lorenz number ratio, $L_{Th}(T)/L_0$, considering the predominance of normal processes of electron-phonon and impurity scattering, is given by[40–45]

$$\frac{L_{Th}(T)}{L_0} = \frac{\frac{\rho_{imp}}{A} + \left(\frac{T}{\Theta_D}\right)^5 J_5\left(\frac{\Theta_D}{T}\right)}{\frac{\rho_{imp}}{A} + \left(\frac{T}{\Theta_D}\right)^5 J_5\left(\frac{\Theta_D}{T}\right) + \left[1 + \frac{3}{\pi^2}\left(\frac{k_F}{q_D}\right)^2\left(\frac{\Theta_D}{T}\right)^2 - \frac{1}{2\pi^2}\frac{J_7\left(\frac{\Theta_D}{T}\right)}{J_5\left(\frac{\Theta_D}{T}\right)}\right]} \tag{3}$$

Where, L_0 is the Sommerfeld value of the Lorenz number ($L_0 = 2.44 \times 10^{-8}\ \Omega W K^{-2}$). Here k_F is the Fermi wave vector; Θ_D and q_D are the Debye temperature and wavevector, respectively; the Debye integrals J_n can be expressed as,

$$Jn\left(\frac{\Theta_D}{T}\right) = \int_0^{\Theta_{D/T}} \frac{x^n e^x}{(e^x - 1)^2}\,dx \tag{4}$$

In this equation, k_F/q_D is related to the electron–phonon inelastic small-angle scattering (vertical processes). The Debye wave vector for both films is found to be $q_D = 0.837$ Å^{-1} assuming a sound speed[46] of 9076 m s^{-1} and a Debye temperature[47–49] of $\Theta_D = 580$ K. The Fermi vector for TiN and $Ti_{0.98}Si_{0.02}N$ are 0.293 and 0.747 Å^{-1}, respectively, calculated from[30] $k_F = [3\rho^2\ n]^{\frac{1}{3}}$. In this calculation, we utilize the resistivity and carrier concentration listed in Table 1.

Figure 2f presents the calculations of Equation (3), showing that $L_{Th}/L_0 \approx 1$ for TiN implying that thermal conductivity in TiN is electronically driven, while $L_{Th}/L_0 < 1$ for $Ti_{0.98}Si_{0.02}N$. The calculated electron thermal conductivity also reduces by at least 40% in $Ti_{0.98}Si_{0.02}N$ compared to TiN. The reduced Lorenz number in $Ti_{0.98}Si_{0.02}N$ supports the fact that the phononic contribution in $Ti_{0.98}Si_{0.02}N$ is non-negligible due to the relative similarity in thermal conductivity to the TiN film presented in Figure 2e.

To illustrate this effect further, the electron contribution (κ_{electron}) to thermal conductivity for TiN and $Ti_{0.98}Si_{0.02}N$ across 200 K≤ T ≤400 K is shown in Figure 2g. Compared to TiN, the presence of Si in $Ti_{0.98}Si_{0.02}N$ lowers κ_{electron} through alloy scattering, as Si atoms act as point defects introducing additional, temperature-independent scattering centers. This reduces l_e and conductivity, σ $(= 1/\rho)$, thereby suppressing κ_{electron} as confirmed by Table 1. It is also noted that although electron–phonon scattering intensifies at higher temperatures and is expected to reduce σ, the Wiedemann-Franz relation ($\kappa_{\text{electron}} = L\sigma T$) dictates that the explicit linear dependence on T outweighs the reduction in σ, leading to a net increase in κ_{electron}. This increase in κ_{electron} therefore reflects the balance between stronger scattering and the linear T term, rather than serving as direct microscopic evidence of electron–phonon interactions. The lattice contribution to thermal conductivity (κ_{phonon}) is shown in Figure 2h for TiN and $Ti_{0.98}Si_{0.02}N$ between 200 K≤ T ≤400 K. Overall, κ_{phonon} decreases with increasing temperature due to enhanced phonon-phonon

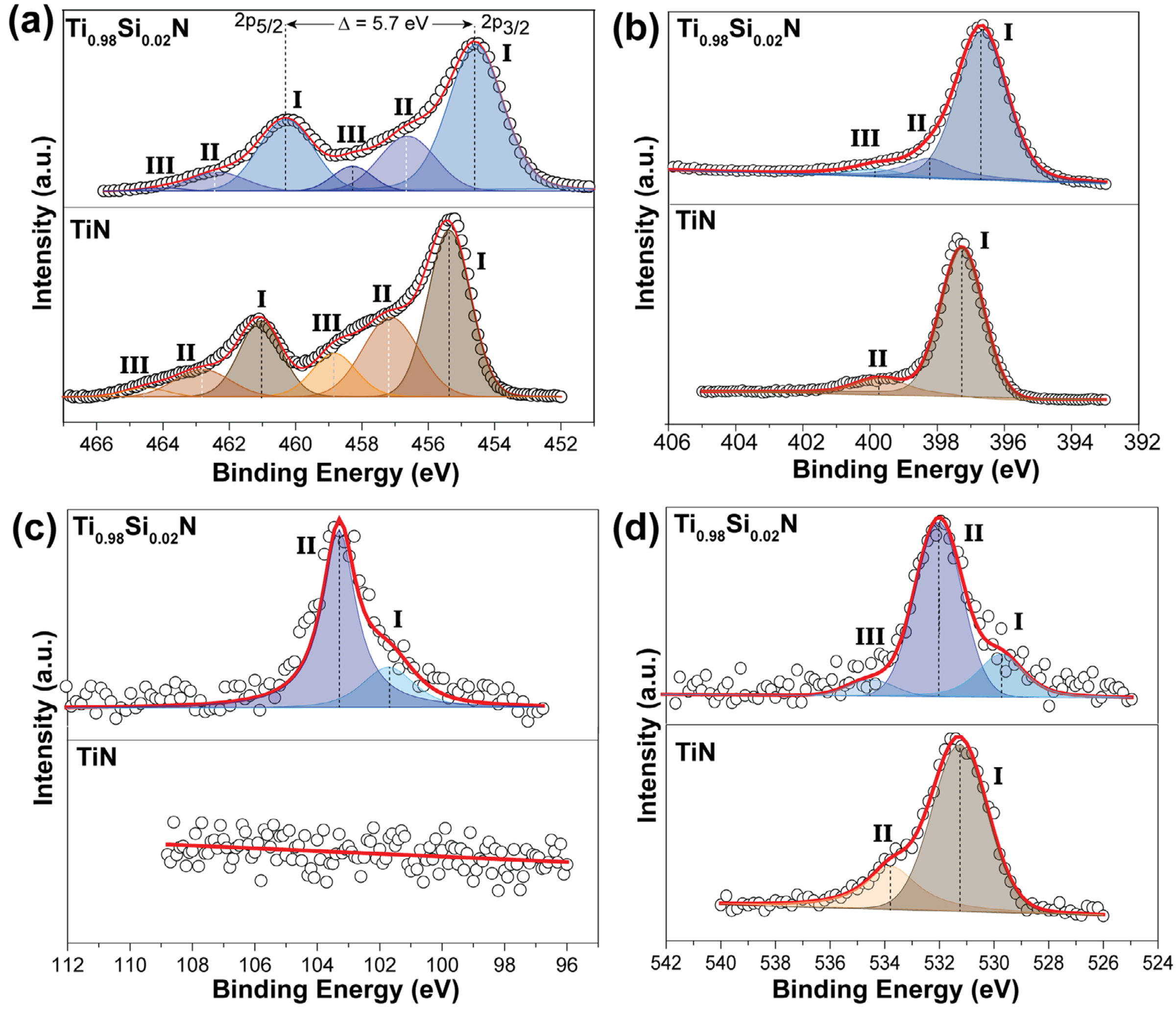

Figure 3. a) XPS fine spectra of Ti 2p for TiN (bottom) and $Ti_{0.98}Si_{0.02}N$ (top). b) XPS fine spectra of N 1s for TiN (bottom) and $Ti_{0.98}Si_{0.02}N$ (top). c) XPS fine spectra of Si 1s for TiN (bottom) and $Ti_{0.98}Si_{0.02}N$ (top). d) XPS fine spectra of O 1s for TiN (bottom) and $Ti_{0.98}Si_{0.02}N$ (top). The deconvoluted peaks designated by roman numerals are described in the text.

Umklapp scattering.[50,51] As temperature rises, the population of high-energy phonons increases, leading to more frequent momentum non-conserving events that shorten the phonon mean free path and reduce κ_{phonon}. Bounded by the uncertainty of the measurements, κ_{phonon} for $Ti_{0.98}Si_{0.02}N$ is higher compared to TiN thus, resulting in comparable κ_{total}.

2.2. Materials Characterization

In **Figure 3**a, XPS fine spectra of Ti 2p are compared for TiN and $Ti_{0.98}Si_{0.02}N$. For TiN, the Ti $2p_{3/2}$ binding energy is at 455.39 eV with a spin-orbit splitting[52] of ≈5.70 eV (Peak I). The peak located at 458.88 eV can be attributed to Ti—O bonds (Peak III). The peak in between and positioned at 457.17 eV represents Ti—N—O (Peak II).[53] The Ti 2p spectrum for $Ti_{0.98}Si_{0.02}N$ shows the Ti $2p_{3/2}$ located at 454.41 eV (Peak I). A peak corresponding to Ti—O is found at 457.68 eV (Peak III), and a Ti—N—O peak is found at 455.98 eV (Peak II). There is no indication of any Ti—Si bonding, in line with our previous work.[21]

The N 1s spectra are shown in Figure 3b. The N—Ti for TiN was centered at 397.26 eV (Peak I). A N—H bond is indicated by a peak[52] at 399.71 eV (Peak II). For $Ti_{0.98}Si_{0.02}N$, the N—Ti peak is centered at 396.65 eV (Peak I) and the N—H peak is centered at 399.80 eV (Peak III). A N—Si bond is also found centered at 398.21 eV (Peak II) that is not present in the TiN spectrum.

The Si 2p spectra are shown in Figure 3c. No Si is detected in TiN. For $Ti_{0.98}Si_{0.02}N$, Si—N bonding is observed[54] at 101.72 eV (Peak I) in line with the N—Si signature seen in Figure 3b. In addition, the Si—O peak[52] is found to be at 103.31 eV (Peak II). Comparing the area under the deconvolved peaks for the Si—N (area of 50) and Si—O (area of 160), it appears that the Si—O is more dominant in the $Ti_{0.98}Si_{0.02}N$ films. Finally, in Figure 3d, the O1s spectrum for TiN shows an O—Ti peak[55] at 531.26 eV (Peak I) and a lesser O—H peak[55] at 533.76 eV (Peak II). The spectrum for $Ti_{0.98}Si_{0.02}N$ has the O—Ti peak at 529.75 eV (Peak I) and the O—H peak at 534.51 eV (Peak III). Mirroring the Si 2p

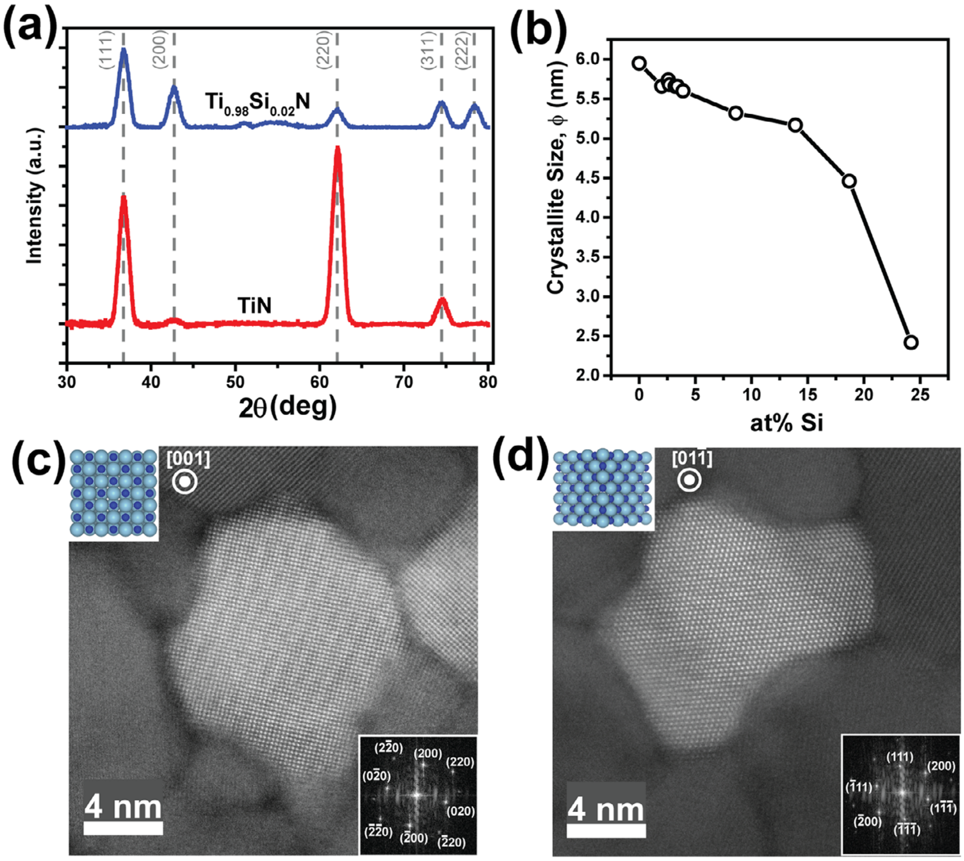

Figure 4. a) XRD of TiN and $Ti_{0.98}Si_{0.02}N$, b) Crystallite size as a function of at% Si obtained from XRD data using the Scherrer equation. c) HAADF TEM image of a TiN grain. The lower inset shows the fast Fourier transform (FFT) of the grain. The FFT pattern corresponds to [001] oriented grain shown as the top inset. d) HAADF TEM image of a $Ti_{0.98}Si_{0.02}N$ grain. The lower inset shows the FFT of the grain. The FFT pattern corresponds to [01$\bar{1}$] oriented grain shown as top inset.

spectrum in Figure 3c, the O—Si peak dominates and is centered at 532.03 eV (Peak II).[52]

Thus, while the O binds to Ti in TiN films, the presence of 2 at% Si in the film causes the O to redistribute by bonding with both Ti and Si. Since the Gibbs free energy of formation for SiO_2 and TiO_2 is similar, the propensity for O to bond to Si could be related to the difficulty of replacing the Ti—N bonds with Ti—O bonds.

Figure 4a shows the XRD pattern for TiN and $Ti_{0.98}Si_{0.02}N$. TiN crystallizes as a face-centered cubic (fcc) structure, and the diffraction peaks were identified according to JCPDS 38-1420. We note that the lattice parameter for the fcc TiN crystal structure is 0.424 nm. For TiN, the two strongest peaks are identified as (111) and (220). For $Ti_{0.98}Si_{0.02}N$, the (200) peak intensity increases relative to (111) and (220). The change in peak intensities from (111) preferred to (200) preferred has been reported in literature for $Ti_{1-x}Si_xN$ films.[54,56] Patscheider et al., have reported amounts as small as 1–3 at% Si added can lead to a loss (111) orientation, which is a charge-neutral plane.[56] This behavior can be attributed to the Si restricting the growth of TiN grains with (111) orientation. Additionally, no peak shifts are seen upon Si addition, indicating little to no Si-based strain in the TiN lattice. This result is surprising given that the ionic radius[3–6,8–12,16–20,22–26,57] for Ti^{3+} (at a coordination number, CN = 6) is 61.7 pm, whereas for Si^{4+} (CN = 6) is 40.0 pm. A substitution of Si^{4+} for Ti^{3+}, therefore seems unlikely and will be further clarified when describing transmission electron microscopy (TEM) results.

The crystallite (grain) size "ϕ" is determined using the Scherrer equation as, $\phi = \frac{K\lambda}{\beta \cos\theta}$. Here, K is the shape factor = 0.94, λ is the wavelength of the X-ray (Cu Kα = 0.154 nm), β is the full width half maximum (FWHM) of the peak, and θ is the Bragg angle. The error in estimated grain diameter cannot be clearly quantified here, as every method of determining crystal size yields a different estimated diameter.[58] Figure 4b indicates decreasing grain size with increased Si content. For TiN, the crystallite size is 5.95 nm, while for $Ti_{0.98}Si_{0.02}N$ the crystallite size is 5.66 nm. At the highest Si content, 24.2%, the crystallite size reduces to 2.42 nm.

Figure 4c shows a high-resolution TEM (HRTEM) of a representative TiN grain. The FFT in the inset of the grain shows cubic symmetry and matches the fcc crystal structure with [001] zone axis in line with XRD. Figure 4d shows HRTEM of the $Ti_{0.98}Si_{0.02}N$ film. The FFT of the grain shows hexagonal symmetry and matches the fcc crystal structure with [01$\bar{1}$] zone axis in line with XRD.

From the wide field-of-view scanning transmission electron microscopy (STEM) image **Figure** 5a, the average grain size for TiN is 5.99 ± 1.63 nm in line with XRD data above. STEM

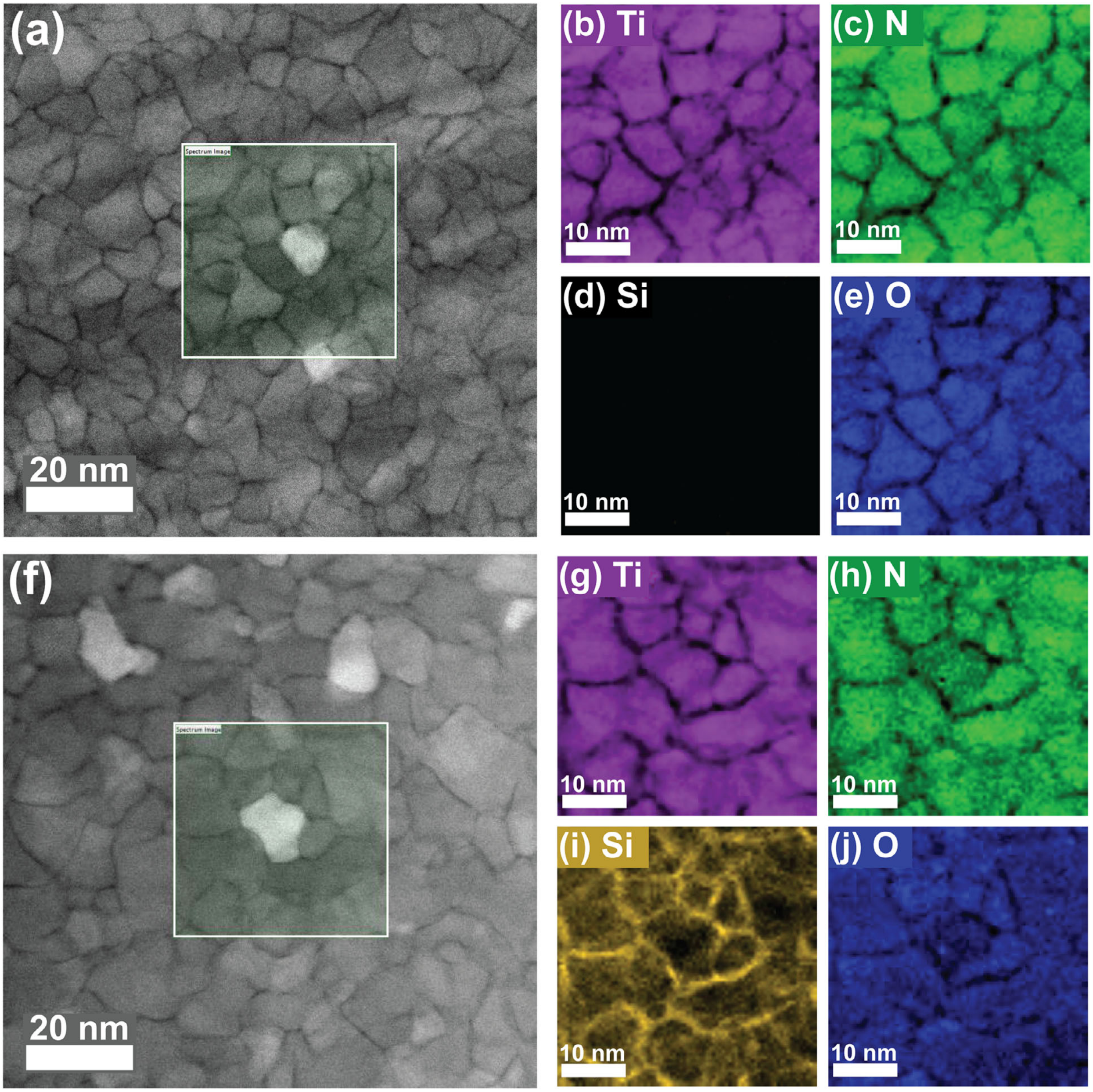

Figure 5. STEM EELS analysis of TiN: a) Low magnification image showing the boxed region analyzed for EELS. Elemental maps for b) Ti, c) N, d) Si, and e) O. STEM EELS analysis of $Ti_{0.98}Si_{0.02}N$; f) Low mag image showing boxed region analyzed for EELS. Elemental maps for g) Ti h) N i) Si, and j) O. The primary difference in the two samples is observed in the Si mapping, where most of the Si is observed as segregated to the grain boundaries.

electron energy loss spectroscopy (EELS) mapping of TiN is shown in Figure 5b–e. Ti and N appear to be uniformly distributed. The O can also be detected as well and is uniformly distributed. As expected, the elemental mapping reveals no presence of Si. In Figure 5f, a large field of view for the $Ti_{0.98}Si_{0.02}N$ sample is shown with an average grain size of 5.75 ± 1.85 nm. Figure 5g–j shows $Ti_{0.98}Si_{0.02}N$ elemental distribution for Ti, N, O, and Si.

The most striking aspect of the EELS is the Si elemental map, where Si is observed decorating the grain boundaries. This observation is also shown for Cu[59] and Ni-doped TiN.[60] The cations tend to reside in the grain boundaries lowering their energy as lattice strains are better accommodated in these disordered regions. These cations further present energetic barriers for dislocation motion thus, "pinning" the dislocations and preventing grain growth.

2.3. Density Functional Theory (DFT) Calculations and Modeling

Out of the 21 different configurations of TiN unit cells with Si and O inserted (Figure S1, Supporting Information), all but three instances yielded metallic behavior (Table S1 and Figure S2, Supporting Information), supporting the idea of TCR >0 in

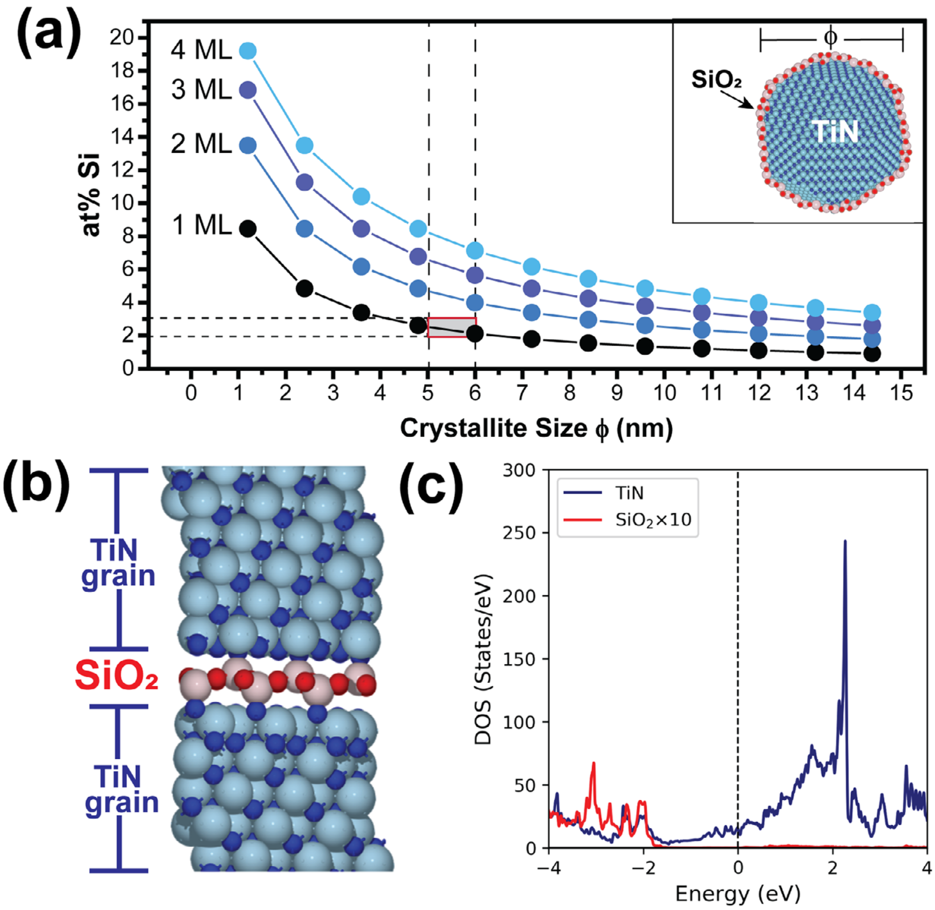

Figure 6. a) Variation of at% Si with SiO$_2$ shell covering TiN crystal. Each curve represents the addition of one monolayer (ML) to the SiO$_2$ shell. The red boxed region shows the likeliest SiO$_2$ shell thickness of ≈1 ML, given, 5 nm$\leq \varphi \leq$6 nm and 2$\leq$ at% Si $\leq$3. b) Schematic of the proposed grain edge with 1 ML of SiO$_2$ inserted between two TiN grains. The structure shown is fully relaxed (ionic relaxation) and shows in-plane Si—O bonds with out-of-plane Si—N bonds to adjacent TiN grains. c) Density of states (DOS) calculated for the structure in (b), demonstrating the presence of finite DOS at the Fermi level (i.e., at $E = 0$ eV) and therefore, metallic conductivity.

the Ti—Si—N system. For these three cases, DFT calculations indicate that a direct Si to O bonding is a necessary requirement for bandgap opening, supporting the experimental observation from XPS where the Si preferentially bonds with O. Furthermore, the EELS data shows evidence that the Si is present at the grain boundaries.

Using this information, we have constructed a geometric model which consists of a TiN nanocrystal with a conformal layer of SiO$_2$ on the surface. It is likely that such a layer may exist as SiO$_{2\text{-x}}$ though experimental observation is challenging. **Figure 6a** shows a series of trend lines with the variation of at% Si vs “ϕ,” for varying monolayers (ML) of SiO$_2$. Under the assumption of a conformal coverage, it can be seen that for Si of 2–3 at%, there can only be 1 ML of SiO$_2$ that can cover a 5–6 nm grain, shown as a red boxed region. Therefore, the idealized grain boundary can be constructed as shown in Figure 6b, where two grains of TiN are separated by 1 ML of SiO$_2$. The structure, as fully relaxed, shows in-plane Si—O bonds and out-of-plane Si—N bonds. The calculated electron density of states (DOS) of the system in Figure 6c shows a finite DOS at the Fermi level, indicative of metallic conductivity. As expected, the origin of the finite DOS is the TiN, as also evidenced by a slightly positive TCR for many films with 2$\leq$ at% Si $\leq$4 (Figure 1b, inset). Such a structure is amenable to direct tunneling.[61] Increasing the Si at% to $\geq$4 at% leads to further Si grain boundary segregation, i.e., a thicker SiO$_2$ layer and results in an increase in resistance leading to a TCR $<$0.

3. Discussion

We contextualize our experimental results within the framework proposed by Kaveh and Mott for disordered metals for predicting the temperature dependence of conductivity.[62] Such an approach for Ti$_{0.98}$Si$_{0.02}$N films can be justified given the nanocrystalline nature and the grain boundary segregation of Si, which provides a high concentration of scattering centers. Using the Kubo–Greenwood formulation, the conductivity can be related to the Boltzmann conductivity, modulated by a scattering factor which is a probability term that is integrated in k-space with an upper limit given by $q_{max} = \pi/l_e$, where l_e is previously defined in Equation (2) as the elastic mean free path; and a lower limit given by $q_{min} = \pi/L_{max}$. Here, L_{max} is the electron diffusion length given as, $L_{MAX} = (\frac{1}{2} l_e l_{IN})^{1/2}$. Here, l_{IN} is the inelastic mean free path and indicated by our thermal conductivity measurements to play a non-trivial role for $Ti_{0.98}Si_{0.02}N$. The temperature dependence of the conductivity, σ(T) is then given as –

$$\sigma\,(T) = \frac{e^2}{\pi^2 \hbar}\left[\frac{1}{L_{MAX}} - \frac{\left(k_F l_e\right)^2}{3 l_{IN}}\right] \tag{5}$$

Tsuei[63] has evaluated the temperature dependence of the above equation and shown that when TCR ≈0, $l_{IN} = \frac{4}{27}(k_F l_e)^4 l_e$. For $Ti_{0.98}Si_{0.02}N$ given $l_e|_{300K} = 0.712$ nm and the Fermi wave vector at 300 K, $k_F|_{300K} = (3\pi^2 n_{300})^{1/3} = 7.47\ nm^{-1}$; and we get from Equation (5), $l_{IN} = 84.6$ nm. The maximum diffusion length is then given as,

$$L_{MAX} = 5.5\ \text{nm} \tag{6}$$

Thus, our calculations for $Ti_{0.98}Si_{0.02}N$ suggest that there are two limiting length scales (corresponding to q_{max} and q_{min}) for electrons to experience scattering. One is given by l_e (0.712 nm) which, as previously stated, approaches the lattice constant of 0.424 nm and leads to the MIR limit being satisfied. The second length scale is given by L_{MAX} (5.5 nm), which is the effective electron diffusion length. This value is remarkably close to the crystallite size (5.66 nm from XRD) of the $Ti_{0.98}Si_{0.02}N$.

The close correlation of the lower and upper bounds of electron scattering to structural parameters in the $Ti_{0.98}Si_{0.02}N$ film points to two unique aspects of our work. From a synthesis perspective, we demonstrate a rationally designed mixed nitride film where the precise addition of Si segregates at the grain boundary, limits grain growth, and "getters" intrinsic O from the TiN matrix. From a physics perspective, we show that the length scales for electron scattering, i.e., electron elastic mean free path and the electron diffusion length closely relate to two of the structural characteristic lengths, i.e., lattice parameter and the grain size, of the $Ti_{0.98}Si_{0.02}N$ films, thus providing robust temperature-invariant resistivity.

4. Conclusion

In summary, we demonstrate that atomic-layer-deposited $Ti_{0.98}Si_{0.02}N$ films achieve an ultralow temperature coefficient of resistivity (0.05 ppm K^{-1}) across an exceptionally broad temperature range (80–420 K). This stability arises from a scattering mechanism governed by Si doping, where Si segregates to grain boundaries; confines crystallite sizes to 5.66 nm, and getters O from the TiN matrix. This results in increased charge carrier concentration and reduced mobility. Crucially, the elastic mean free path (0.712 nm) approaches the lattice parameter (0.424 nm), and the electron diffusion length (5.5 nm) is similar to the crystallite size, creating a temperature-invariant scattering regime bounded by these structural dimensions. Thus, by leveraging a combination of precise atomic doping and mesoscale grain boundary engineering, our findings in a mixed nitride conductor establish a design paradigm for materials to demonstrate highly stable, near-zero temperature coefficient of resistivity.

5. Experimental Section

Atomic Layer Deposition (ALD): All films were deposited by ALD on the Eugenus 300 mm commercial QXP 8300 mini-batch system. The substrates used were 1000 Å of SiO_2 on Si (100). The TiN was deposited at 450 °C using titanium tetrachloride ($TiCl_4$) and ammonia (NH_3). The Ti—Si—N films were also deposited at 450 °C using $TiCl_4$, NH_3, and dichlorosilane (DCS). The target film thickness on all samples was 120–150 nm, as measured by X-ray reflectometry (XRR). Dose saturation for the precursors was achieved at a few seconds each. The deposition pressure was maintained in the 1–7 Torr range. The different levels of silicon incorporation were achieved by varying the number of DCS pulses added to the $TiCl_4/NH_3$ process. This information is a part of proprietary Eugenus recipes. In this work, the nomenclature used to label the films is $Ti_{[1-(x/100)]}Si_{x/100}N$, with at. % Si, measured via XPS.

Characterization: Temperature-dependent van der Pauw (vdP) resistivity measurements were conducted using a JanisST500-1-2CX commercial probe station with gold-plated tungsten probe tips of 200 µm tip diameter. Details of the set-up are provided in multiple past publications.[21,64,65] Briefly, samples in triplicate were used to get average statistics for each Ti-Si-N film composition. Indium dots were pressed into the four corners of the film to serve as electrodes for probe placement. A Keithley2400 source meter supplied a constant 100 µA current across two adjacent contacts, and voltage was measured across the other two. The Resistivities of the films were measured over a temperature range from 80 to 420 K in 10 K intervals with an average pressure ≈120 × 10^{-3} Torr.

Room temperature Hall measurements were performed under magnetic fields of 0.2135 and −0.2135 T. The Hall voltage (V_H) was measured by applying current to opposite corners of the sample, 1 and 3, and the voltage was measured across the remaining terminals, 2 and 4 (V_{24}). This measurement was repeated for V_{42}, V_{13}, and V_{31}. All four of these voltages were measured at both positive and negative magnetic fields. V_H was calculated by subtracting the voltages in the negative magnetic field from their counterparts in the positive magnetic field, subsequently summing those voltages, and dividing by eight. From there, carrier concentration was calculated using,

$$n = \frac{IB}{qV_H t} \tag{7}$$

where, *I* is the applied current of 100 mA, *B* is the magnetic field in Tesla, *q* is the electron charge, and *t* is the film thickness in cm. Hall carrier mobility (μ_H) was also calculated from V_H using,

$$\mu_H = \frac{V_H t}{IB\rho} \tag{8}$$

TDTR was used to measure thermal conductivity and related parameters for Ti-Si-N films. This technique relies on a laser-based pump-probe approach in which one laser source was used to provide a localized and modulated heating event to the sample, causing perturbative temperature fluctuations on the sample surface, while a secondary laser source probes the change in reflectivity due to this pump thermal perturbation. The change in probe beam reflectivity was related to the temperature change on the sample surface, which is in turn related to the thermal resistance giving rise to the thermal gradient induced by the pump heater. This thermal gradient was impacted by the Ti-Si-N film, and this thermal resistance was determined based on a multilayer thermal models rooted in the cylindrical heat equation.[66] A TDTR set-up consisted of a Ti: Sapphire laser (Spectra Physics Tsunami) with a central wavelength of ≈808 nm operated at 80 MHz repetition rate was spilt into a pump beam and a probe beam via a two-tint configuration discussed elsewhere.[67–69] The pump beam was modulated at a frequency of 8.4 MHz employing an electro-optic modulator (EOM) in its path. This beam modulation produced a periodic temperature rise on the surface of a sample which changed its reflectivity. A balanced photodetector and a lock-in amplifier were used to detect the change in reflectivity of the sample surface induced at the pump modulation frequency. To convert the optical energy to thermal energy, an 80 nm Al transducer was deposited on the sample surface. Pump and probe beams were focused coaxially to 20 and 10 µm diameters, respectively, on the sample surface by passing through a 10× objective. TDTR constants used for calibration and modeling are provided in Section S2 and Table S2 (Supporting Information). TDTR sensitivity analysis and theoretical fit to experimental data is provided in Section S2 and Figure S3 (Supporting Information).

XPS was carried out using a ThermoFisher Scientific K-Alpha+ XPS system. The X-ray source used was a monochromated Al Kα beam (1486.6 eV). Charge compensation was not used for the samples, as the low Si content was such that the samples were still conducting. The samples were sputtered at a rate of 0.2 nm s^{-1} to clean the surface. The at% Si of the samples was determined at an etch level of 2 nm and normalized without considering the O content in the film. Spectra were shifted relative to a charge reference of adventitious carbon at 284.8 eV. XRD was conducted on a Bruker JV-DX with a wavelength of Cu Kα = 1.54 Å was used. The scans were used to determine crystallinity of the films, as well as crystallite size via the Scherrer equation.[70] Room temperature measurements were made under atmospheric pressure. This tool uses a Soller slit, which limits the spread of the X-ray beam, incident and refracted, to improve the signal-to-noise (S/N) ratio. The presence of the slit must be accounted for when making Scherrer calculations.[71] This correction had been made by the software on the tool automatically. TEM and EELS measurements were done using a JEOL ARM-200F to image the grains and determine elemental distribution. The tool had an accelerating voltage of 200 keV, with a TEM resolution of 0.19 nm and an EELS energy resolution of 0.4 eV. The samples were prepared for TEM using a focused ion beam (FIB) system, Thermo Fisher Helios G4. ImageJ software was used to analyze the TEM images.

Density Functional Theory (DFT): DFT calculations were performed using the Vienna ab initio Simulations Package (VASP),[72,73] employing the projector augmented wave (PAW)[74,75] method and plane-wave basis set. The Perdew–Burke–Ernzerof (PBE)[76,77] functional was used within the generalized gradient approximation (GGA) for describing the exchange-correlation of electrons. A cutoff of 450 eV was set for plane-wave expansion to achieve a total energy convergence within 1 meV atom^{-1}. The valence electron configurations for Ti, N, Si, and O are $3d^24s^2$, $2s^22p^3$, $3s^23p^2$, and $2s^22p^4$, respectively. The Brillouin Zone of the primitive unit cell of TiN was sampled with a Monkhorst-Pack grid[78] of (17 × 17 × 17) for geometry optimization, and (27 × 27 × 27) for calculating electronic density of states (DOS). For modeling the SiO_2 grain boundary in TiN (Figure 4b), 8 layers of $\sqrt{3} \times \sqrt{3}$ TiN(001) slab, and 1 layer of SiO_2 were used. The Brillouin Zone was sampled with a 9 × 9 × 2 grid for structural optimization and 18 × 18 × 4 for DOS calculation. All structures were optimized using a conjugated gradient approach until the residual forces on each atom (ionic core) became smaller than 0.01 eV Å^{-1}.

Supporting Information

Supporting Information is available from the Wiley Online Library or from the author.

Acknowledgements

C.F. was supported by National Science Foundation Grant Number 1908167. The XPS work was supported via an NSF MRI award, Grant Number 1726636. SNB was partially supported by Semiconductor Research Corporation, Grant number 3026.001. MdRI and PEH were primarily supported as part of APEX (A Center for Power Electronics Materials and Manufacturing Exploration), an Energy Frontier Research Center funded by the U.S. Department of Energy, Office of Science, Basic Energy Sciences under Award # ERW0345 (thermal conductivity measurements). In addition, MdRI acknowledges support from the Semiconductor Research Corporation, Grant Number 2025-NM-3286 (thermal analysis). DFT calculations by J.S., D.L., and T.S.R. were supported by the Department of Energy grant DE-FG02-07ER46354. Computational resources were provided by the National Energy Research Scientific Computing Center (NERSC).

Conflict of Interest

The authors declare no conflict of interest.

Data Availability Statement

The data that support the findings of this study are available from the corresponding author upon reasonable request.

Keywords

atomic layer deposition (ALD), near-zero temperature coefficient of resistivity (nz-TCR), time-domain thermoreflectance (TDTR), TiSiN

Received: July 27, 2025
Revised: October 29, 2025
Published online: November 11, 2025

---

[1] H. A. Schafft, J. S. Suehle, *Solid-State Electron.* **1992**, *35*, 403.
[2] P. L. Rossiter, in *The Electrical Resistivity of Metals and Alloys*, Cambridge University Press, Cambridge, England **1987**.
[3] R. Goldstein, J. Szwarc, in *2001 51st Electronic Components and Technology Conf.*, Orlando, FL, USA, May **2001**.
[4] S. Deng, Y. Sun, L. Wang, H. Wu, K. Shi, P. Hu, Q. Huang, C. Wang, *Appl. Phys. Lett.* **2016**, *108*, 041908.
[5] L. Ding, C. Wang, L. Chu, J. Yan, Y. Na, Q. Huang, X. Chen, *Appl. Phys. Lett.* **2011**, *99*, 251905.
[6] K. Takenaka, A. Ozawa, T. Shibayama, N. Kaneko, T. Oe, C. Urano, *Appl. Phys. Lett.* **2011**, *98*, 022103.
[7] J. Van Den Broek, J. Donkers, R. Van Der Rijt, J. Janssen, *Philips J. Res.* **1998**, *51*, 429.
[8] Y. T. Kim, *Appl. Phys. Lett.* **1997**, *70*, 209.
[9] I. Krylov, Y. Qi, V. Korchnoy, K. Weinfeld, M. Eizenberg, E. Yalon, *Appl. Phys. Lett.* **2020**, *117*, 041902.
[10] B. Fu, L. Gao, *Scr. Mater.* **2006**, *55*, 521.
[11] B. C. Marin, S. E. Root, A. D. Urbina, E. Aklile, R. Miller, A. V. Zaretski, D. J. Lipomi, *ACS Omega* **2017**, *2*, 626.
[12] T. Park, H. K. Woo, B. K. Jung, B. Park, J. Bang, W. Kim, S. Jeon, J. Ahn, Y. Lee, Y. M. Lee, T.-I. Kim, S. J. Oh, *ACS Nano* **2021**, *15*, 8120.
[13] J. H. Mooij, *Phys. Stat. Sol. (a)* **1973**, *17*, 521.
[14] A. F. Ioffe, A. R. Regel, *Prog. Semicond.* **1960**, *4*, 237.
[15] N. F. Mott, *Phil. Mag.* **1972**, *26*, 1015.
[16] Y. Dai, X. Wu, D. Guo, Z. Sun, *Appl. Phys. A* **2022**, *128*, 851.
[17] H. Kino, T. Fukushima, T. Tanaka, *Appl. Phys. Express* **2021**, *14*, 091003.
[18] P. Sun, M. Zhu, K. Wang, M. Zhong, J. Wei, D. Wu, H. Zhu, *ACS Appl. Mater. Interfaces* **2013**, *5*, 9563.
[19] J. C. Lin, P. Tong, S. Lin, B. S. Wang, W. H. Song, Y. P. Sun, *J. Appl. Phys.* **2014**, *116*, 213912.
[20] S.-G. Hur, D.-J. Kim, B.-D. Kang, S.-G. Yoon, *J. Vac. Sci. Technol. B* **2004**, *22*, 2698.
[21] C. Feit, S. Chugh, A. R. Dhamdhere, H. Y. Kim, S. Dabas, S. J. Rathi, N. Mukherjee, P. Banerjee, *J. Vac. Sci. Technol. A* **2020**, *38*, 062404.
[22] S. Lee, E.-M. Kim, Y. Lim, *Sci. Rep.* **2019**, *9*, 7763.
[23] I.-S. Park, S.-Y. Park, G.-H. Jeong, S.-M. Na, S.-J. Suh, *Thin Solid Films* **2008**, *516*, 5409.
[24] M.-Y. Cho, D.-W. Lee, W.-J. Kim, Y.-N. Kim, S.-M. Koo, D. Lee, K.-S. Moon, J.-M. Oh, *Ceram. Int.* **2018**, *44*, 18736.
[25] H. Li, G. Wang, P. Hu, D. Li, S. Dang, X. Ma, T. Dai, S. Kang, F. Yu, X. Zhou, S. Wu, S. Li, *J. Appl. Phys.* **2018**, *124*, 093903.
[26] S.-K. Chen, Y.-F. Kao, *AIP Adv.* **2012**, *2*, 012111.
[27] C. J. K. Richardson, A. Alexander, C. G. Weddle, B. Arey, M. Olszta, *J. Appl. Phys.* **2020**, *127*, 235302.

[28] C.-H. Kuo, V. Wang, Z. Zhang, J. Spiegelman, D. Alvarez, A. C. Kummel, S. Yun, H. Simka, presented at *2021 IEEE International Interconnect Technology Conference (IITC)*, Kyoto, Japan, July **2021**.

[29] E. O. Chi, W. S. Kim, N. H. Hur, *Solid State Commun.* **2001**, *120*, 307.

[30] N. W. Ashcroft, N. D. Mermin, in *Solid State Physics*, Holt, Rinehart and Winston, New York **1976**.

[31] B. O. Johansson, J. E. Sundgren, J. E. Greene, A. Rockett, S. A. Barnett, *J. Vac. Sci. Technol. A* **1985**, *3*, 303.

[32] D. Gall, I. Petrov, J. E. Greene, *J. Appl. Phys.* **2001**, *89*, 401.

[33] P. Patsalas, S. Logothetidis, *J. Appl. Phys.* **2001**, *90*, 4725.

[34] B. F. Donovan, E. Sachet, J.-P. Maria, P. E. Hopkins, *Appl. Phys. Lett.* **2016**, *108*, 021901.

[35] E. A. Scott, K. Hattar, C. M. Rost, J. T. Gaskins, M. Fazli, C. Ganski, C. Li, T. Bai, Y. Wang, K. Esfarjani, M. Goorsky, P. E. Hopkins, *Phys. Rev. Mater.* **2018**, *2*, 095001.

[36] A. Giri, J. L. Braun, C. M. Rost, P. E. Hopkins, *Scr. Mater.* **2017**, *138*, 134.

[37] R. E. Taylor, *J. Am. Ceram. Soc.* **1962**, *45*, 353.

[38] R. E. Taylor, *J. Am. Ceram. Soc.* **1961**, *44*, 525.

[39] R. E. Taylor, J. Morreale, *J. Am. Ceram. Soc.* **1964**, *47*, 69.

[40] R. E. B. Makinson, *Math. Proc. Cambridge Philos. Soc.* **1938**, *34*, 474.

[41] A. H. Wilson, *Math. Proc. Cambridge Philos. Soc.* **1937**, *33*, 371.

[42] Q. Zheng, A. B. Mei, M. Tuteja, D. G. Sangiovanni, L. Hultman, I. Petrov, J. E. Greene, D. G. Cahill, *Phys. Rev. Mater.* **2017**, *1*, 065002.

[43] S. J. Mason, D. J. Wesenberg, A. Hojem, M. Manno, C. Leighton, B. L. Zink, *Phys. Rev. Mater.* **2020**, *4*, 065003.

[44] P. G. Klemens, R. K. Williams, *Int. Met. Rev.* **1986**, *31*, 197.

[45] T. M. Tritt, *ChemInform* **2012**, *43*, 201210227.

[46] W. J. Meng, G. L. Eesley, *Thin Solid Films* **1995**, *271*, 108.

[47] D. W. Field, *Phys. Stat. Sol. (B)* **1984**, *123*, 479.

[48] E. Mohammadpour, M. Altarawneh, J. Al-Nu'airat, Z.-T. Jiang, N. Mondinos, B. Z. Dlugogorski, *Mol. Simul.* **2018**, *44*, 415.

[49] D. Chen, J. Chen, Y. Zhao, B. Yu, C. Wang, D. Shi, *Acta Metall. Sin. (Engl. Lett.)* **2009**, *22*, 146.

[50] P. E. Hopkins, J. A. Tomko, A. Giri, *J. Appl. Phys.* **2022**, *131*, 015101.

[51] B. M. Foley, E. A. Paisley, C. DiAntonio, T. Chavez, M. Blea-Kirby, G. Brennecka, J. T. Gaskins, J. F. Ihlefeld, P. E. Hopkins, *J. Appl. Phys.* **2017**, *121*, 205104.

[52] J. F. Moulder, W. F. Stickle, P. E. Sobol, K. D. Bomben, in *Handbook of X-Ray Photoelectron Spectroscopy*, Perkin-Elmer, Eden Prairie, MN, USA **1995**, pp. 230–232.

[53] P. Korusenko, S. Nesov, S. Povoroznyuk, P. Orlov, D. Korotaev, K. Poleshenko, E. Tarasov, *Data Brief* **2019**, *27*, 104737.

[54] T. Kimura, R. Yoshida, K. Azuma, *IEEE Trans. Plasma Sci.* **2021**, *49*, 53.

[55] M. J. Jackman, A. G. Thomas, C. Muryn, *J. Phys. Chem. C* **2015**, *119*, 13682.

[56] J. Patscheider, T. Zehnder, M. Diserens, *Surf. Coat. Technol.* **2001**, *146–147*, 201.

[57] R. D. Shannon, *Acta Crystallogr. A* **1976**, *32*, 751.

[58] P. E. Tomaszewski, *Phase Transitions* **2013**, *86*, 260.

[59] Q. Li, T. Guo, L. Liu, X. Wang, K. Gao, X. Pang, *Surf. Coat. Technol.* **2023**, *452*, 129112.

[60] W. Li, P. Liu, S. Zhao, K. Zhang, F. Ma, X. Liu, X. Chen, D. He, *J. Alloys Compd.* **2017**, *691*, 159.

[61] D. A. Muller, T. Sorsch, S. Moccio, F. H. Baumann, K. Evans-Lutterodt, G. Timp, *Nature* **1999**, *399*, 758.

[62] M. Kaveh, N. F. Mott, *J. Phys. C: Solid State Phys.* **1982**, *15*, L707.

[63] C. C. Tsuei, *Phys. Rev. Lett.* **1986**, *57*, 1943.

[64] Z. N. Gao, Y. Myung, X. Huang, R. Kanjolia, J. Park, R. Mishra, P. Banerjee, *Adv. Mater. Interfaces* **2016**, *3*, 1600496.

[65] Z. N. Gao, D. Le, A. Khaniya, C. L. Dezelah, J. Woodruff, R. K. Kanjolia, W. E. Kaden, T. S. Rahman, P. Banerjee, *Chem. Mat.* **2019**, *31*, 1304.

[66] D. G. Cahill, *Rev. Sci. Instrum.* **2004**, *75*, 5119.

[67] K. Kang, Y. K. Koh, C. Chiritescu, X. Zheng, D. G. Cahill, *Rev. Sci. Instrum.* **2008**, *79*, 114901.

[68] M. R. Islam, P. Karna, J. A. Tomko, E. R. Hoglund, D. M. Hirt, M. S. B. Hoque, S. Zare, K. Aryana, T. W. Pfeifer, C. Jezewski, A. Giri, C. D. Landon, S. W. King, P. E. Hopkins, *Nat. Commun.* **2024**, *15*, 9167.

[69] D. Hirt, M. R. Islam, M. S. B. Hoque, W. Hutchins, S. Makarem, M. K. Lenox, W. T. Riffe, J. F. Ihlefeld, E. A. Scott, G. Esteves, P. E. Hopkins, *Appl. Phys. Lett.* **2024**, *124*, 202202.

[70] A. S. Vorokh, *Nanosyst.: Phys. Chem. Math.* **2018**, *9*, 364.

[71] H. M. Otte, *J. Appl. Phys.* **2004**, *32*, 1536.

[72] G. Kresse, J. Furthmüller, *Phys. Rev. B* **1996**, *54*, 11169.

[73] G. Kresse, J. Furthmuller, *Comp. Mater. Sci.* **1996**, *6*, 15.

[74] P. E. Blöchl, *Phys. Rev. B* **1994**, *50*, 17953.

[75] G. Kresse, D. Joubert, *Phys. Rev. B* **1999**, *59*, 1758.

[76] J. P. Perdew, K. Burke, M. Ernzerhof, *Phys. Rev. Lett.* **1996**, *77*, 3865.

[77] J. P. Perdew, K. Burke, M. Ernzerhof, *Phys. Rev. Lett.* **1997**, *78*, 1396.

[78] H. J. Monkhorst, J. D. Pack, *Phys. Rev. B* **1976**, *13*, 5188.